On the resolution-dependence of cloud fraction in radiative-convective equilibrium

Nadir Jeevanjee[1], **Linjiong Zhou**[1]

[1]Geophysical Fluid Dynamics Laboratory, Princeton NJ, 08540

Key Points:

- Cloud-resolving simulations of radiative-convective equilibrium exhibit a marked increase of anvil cloud fraction with resolution.
- This sensitivity is closely related to the resolution-dependence of evaporation and precipitation efficiency
- The root of these sensitivities is the resolution-dependence of mixing between clear and cloudy air

Corresponding author: Nadir Jeevanjee, nadir.jeevanjee@noaa.gov

Abstract

Tropical anvil clouds are an important player in Earth's climate and climate sensitivity, but simulations of anvil clouds are uncertain. Here we pinpoint one source of uncertainty by demonstrating a marked increase of anvil cloud fraction with resolution in cloud-resolving simulations of radiative-convective equilibrium. This increase in cloud fraction can be traced back to the resolution dependence of horizontal mixing between clear and cloudy air. A mixing timescale is diagnosed for each simulation using the cloud fraction theory of *Seeley et al.* [2019] and is found to scale linearly with grid spacing, as expected from a simple scaling law. Thus mixing becomes more efficient with increasing resolution, generating more evaporation, decreased precipitation efficiency, greater mass flux, and hence greater detrainment and cloud fraction. The decrease in precipitation efficiency also yields a marked increase in relative humidity with resolution.

1 Introduction

Tropical anvil clouds exert considerable leverage over the Earth's radiation budget, by reflecting sunlight as well as trapping thermal infrared radiation [e.g. *Hartmann et al.*, 2001]. Any change in anvil cloud area with warming is thus a potentially significant climate feedback [*Lindzen et al.*, 2001; *Mauritsen and Stevens*, 2015]. Indeed, this 'tropical anvil cloud area feedback' was recently assessed by *Sherwood et al.* [2020] to be -0.2 ± 0.2 W/m^2/K, a magnitude (and uncertainty) comparable to other cloud feedbacks, including low-cloud feedbacks.

While tropical anvil clouds and their area feedbacks are thus important players in the climate system, confidence in their simulation is low. Global climate models (GCMs) exhibit a significant spread in climatological anvil cloud fraction [*Cesana and Chepfer*, 2012; *Su et al.*, 2013], as well as an uncertain sign in anvil cloud area feedbacks [*Zelinka et al.*, 2016]. Even cloud resolving models (CRMs) exhibit an uncertain sign in anvil cloud area changes with warming, with some CRMs exhibiting a decrease [*Romps*, 2020; *Cronin and Wing*, 2017] and others exhibiting an increase [*Singh and O'Gorman*, 2015]. Similar ambiguities are found in global-scale, convection-permitting models [*Tsushima et al.*, 2014; *Narenpitak et al.*, 2017]. Such uncertainty led *Sherwood et al.* [2020] to base their assessment of the anvil cloud area feedback almost entirely on observations [*Williams and Pierrehumbert*, 2017]. This uncertainty in modeled anvil cloud area feedback is highlighted and reinforced by the results of the recent Radiative-Convective Equilibrium Model Intercomparison Project [RCEMIP, *Wing et al.*, 2020], which finds a strikingly large spread in both climatological anvil cloud fraction and anvil fraction changes with warming, across both convection-resolving and coarse-resolution simulations (see, e.g., their Fig. 15).

Given the importance of anvil cloud area to climate, as well as the aforementioned uncertainties in their simulation, a deeper study of the fundamental physics of anvil clouds seems warranted. Although divergence and detrainment have long been recognized as key determinants of anvil cloud fraction [*Hartmann and Larson*, 2002], the recently developed formalism of *Seeley et al.* [2019] (hereafter S19) emphasized the additional role of cloud lifetime in determining anvil cloud amount. While the lifetime of a cloudy parcel depends on a number of quantities, a key determinant in the S19 formalism is the characteristic timescale κ with which a volume of cloudy air mixes with an equal volume of clear air. This timescale influences a number of processes, including the rate of condensate evaporation, condensate dilution, and the spreading of anvil clouds.

The S19 formalism, and our physical picture of anvil cloud evolution in general, however, assumes that anvil clouds spread continuously after their detrainment from convective cores. But in simulations of cloud ensembles, such as cloud-resolving RCE, convective cores are typically only a few grid cells wide, even down to resolutions of $O(100\text{ m})$ [*Jeevanjee*, 2017]. Thus, we might expect the spreading of anvil clouds in such simulations to be grid-dependent. Indeed, if the turbulent horizontal wind speed which advects air between grid

cells is u_{rms}, then one expects the timescale κ (with which a cloudy grid cell completely mixes with a neighboring clear grid cell) to scale with horizontal grid spacing dx as

$$\kappa \sim dx/u_{\text{rms}} \ . \tag{1}$$

If this is true, and given the varied and significant influences of κ on cloud fraction, we might then also expect cloud fraction to depend on resolution. We confirm this in Fig. 1 by plotting cloud fraction for a series of cloud-resolving radiative-convective equilibrium (RCE) simulations with dx varying from 0.0625 m to 16 km; details of these simulations are given in Section 2. The left panel shows simulations with the six-class GFDL microphysics scheme [*Zhou et al.*, 2019], while the right panel shows simulations with a Kessler-type warm-rain microphysics scheme [*Kessler*, 1969, details below]. The solid lines show simulations on a fixed grid, whereas dashed lines show simulations with a fixed domain size. A marked increase of high cloud fraction with increasing resolution is evident, and is found in all sets of simulations, suggesting that this result is robust. Similar results were also found with DAM [*Romps*, 2008] (not shown).

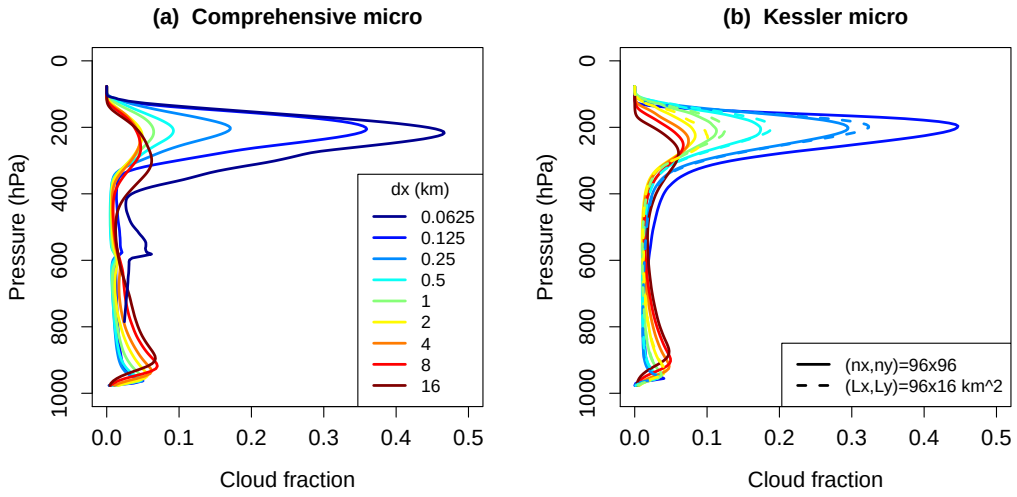

Figure 1. A striking dependence of cloud fraction on resolution Time-mean cloud fraction profiles from FV^3 RCE simulations with varying horizontal resolution (colors). Left panel shows simulations with comprehensive microphysics, while the right panel shows simulations with simplified Kessler microphysics. All simulations are run on a 96 $\times$ 96 horizontal grid, except for those shown in dashed lines which were run on a fixed domain of size 96×16 km^2. Further simulation details are given in Section 2.

This resolution-dependence adds to the aforementioned uncertainties in anvil cloud simulations, and casts further doubt on our ability to simulate anvil clouds with confidence. Furthermore, this decrease in confidence may have unfortunate implications for machine-learning applications in climate models, which sometimes use cloud-resolving simulations as 'ground-truth' training data for AI algorithms [*Rasp et al.*, 2018; *Brenowitz and Bretherton*, 2018; *Yuval and O'Gorman*, 2020]. At the same time, however, a deeper understanding of this resolution sensitivity may lead to a better understanding of our simulations and of anvil cloud dynamics more generally, ideally pointing the way to more accurate simulations and parameterizations.

The goal of this paper is to pursue such understanding. Key components of this pursuit include not only the simulations shown in Fig. 1, but also the theoretical framework of S19, as well as the process-level diagnostics required to utilize the theory. We begin in Section

2 by describing in detail our simulations and these process-level diagnostics. Section 3.1 then formulates a hypothesis for the resolution sensitivity seen in Fig. 1, followed by a brief exposition of the S19 theory in Sections 3.2 and 3.3. Section 4 provides supporting evidence for the hypothesis of Section 3.1. We summarize and conclude in Section 5.

2 Simulations

The atmospheric model used here is the non-hydrostatic version of GFDL's FV^3 [Finite-Volume Cubed-Sphere Dynamical Core, *Harris and Lin*, 2013; *Lin*, 2004]. The simulations analyzed here are very similar, and in some instances the same as, those performed in *Jeevanjee* [2017] (hereafter J17). We give the salient features of our simulations below and refer the reader to J17 for further details, as well as plots and animations depicting the character of the convection in these simulations.

As in J17, a guiding principle in configuring the simulations is to avoid inessential complexity insofar as possible [*Jeevanjee et al.*, 2017]. Thus, we run simple doubly-periodic radiative-convective equilibrium (RCE) simulations over a fixed sea surface temperature of 300 K, at resolutions spanning dx = 0.0625 – 16 km by factors of two. Radiative cooling is non-interactive and is parameterized as a fit to the invariant divergence of radiative flux F found by *Jeevanjee and Romps* [2018]:

$$-\partial_T F = (0.25 \text{ W/m}^2/\text{K}^2) \cdot (T - T_{\text{tp}}) \ . \tag{2}$$

Here the temperature derivative is a vertical derivative, T_{tp} = 200 K is the tropopause temperature, and the above cooling is applied between the surface and 125 hPa, above which temperatures are relaxed to T_{tp} over a timescale of 5 days (so the stratosphere is isothermal). The advantage of this non-interactive radiative cooling is that it is unaffected by the large changes in cloud fraction across our simulations, simplifying their analysis and interpretation. At the same time, cloud-radiation interactions are known to influence anvil and particularly anvil cirrus cloud development [e.g. *Hartmann et al.*, 2018], so future work should investigate how such physics interacts with the mechanisms studied here.

No boundary layer or sub-grid turbulence schemes are used, though small amounts of vorticity and divergence damping are used to stabilize the model and reduce noise. The vertical discretization is Lagrangian [*Lin*, 2004] with 151 levels, and the horizontal grid has 96 points in both x and y, except for the runs shown in dashed lines in Fig. 1. The latter were more expensive, fixed-domain runs which due to computational constraints had a 'bowling-alley' domain of $(L_x, L_y) = 96 \times 16$ km^2 and were run over a smaller resolution range of dx=0.25 – 2 km.

Again in the spirit of avoiding inessential complexity, and to enable use of the theory of *Seeley et al.* [2019], microphysical transformations are performed with a warm-rain version of GFDL microphysics scheme [*Chen and Lin*, 2013] which models only water vapor q_{v}, cloud condensate q_{c}, and rain, with the only transformations being condensation/evaporation of condensate, re-revaporation of rain, and autoconversion of cloud condensate to rain as

$$\left.\frac{dq_{\text{c}}}{dt}\right|_{\text{auto}} = -q_{\text{c}}/t_{\text{aut}} \tag{3}$$

where the autoconversion timescale t_{aut} = 30 minutes. The only exceptions are the simulations shown in Fig. 1a, which use the full complexity (six-class) GFDL microphysics scheme which includes ice processes [*Zhou et al.*, 2019]. While Eq. (3) is extremely idealized, its use seems permissible since comprehensive microphysical processes do not seem essential for understanding how cloud fraction depends on resolution and mixing; indeed, this dependence is very similar for both our warm-rain and full complexity simulations (Fig. 1a).

To analyze convection in our simulations we partition the domain online at each time step into active, inactive, and environmental air. Active (updraft) air has $q_{\text{c}} > q_{\text{c0}} \equiv 10^{-5}$

and vertical velocity $w > w_0$, where w_0 is resolution-dependent (consistent with the findings of J17) and varies between 0.25-1 m/s. Inactive air has $q_c > q_{c0} = 10^{-5}$ and $w < w_0$ and should be thought of as detrained cloud. All other grid points are considered environmental. Cloud fraction C is diagnosed as the fractional area at a given height occupied by active and inactive air. We use this partitioning to conditionally average various quantities (w, q_c, etc.) over these subdomains. We also include microphysical diagnostics of evaporation e, autoconversion a, and condensation c (units kg/m^3/ sec), all of which can also be conditionally averaged as above.

These primary diagnostics, while of interest in their own right, also allow us to derive other diagnostics of interest. One such diagnostic is the convective mass flux $M \equiv \rho w_{up} \sigma_{up}$ (kg/m^2/ sec) where σ_{up} is the fractional area occupied by active updraft air at a given height, and the subscripts "up" and "in" will refer to quantities which are conditionally averaged over active updrafts or inactive air, respectively. Another such diagnostic is the volumetric detrainment $\delta M/\rho$ (1/ sec), where δ is fractional gross detrainment (1/m) and ρ is density. This quantity can be interpreted as the fractional rate at which air at a given height becomes cloudy, and is diagnosed (following *Seeley et al.* [2019]) by considering the cloud water budget for inactive air, which has detrained condensate $\delta M q_{c,up}$ as the sole source term (no condensation) and total evaporation and inactive autoconversion $e + a_{in}$ as sinks. Assuming that sources and sinks balance in steady-state then yields

$$\frac{\delta M}{\rho} = \frac{e + a_{in}}{\rho q_{c,up}} \,. \tag{4}$$

The right-hand side of this equation may be diagnosed from the simulations, yielding a method for diagnosing $\delta M/\rho$. Since M and ρ can also be diagnosed independently, this also yields a method for diagnosing the fractional detrainment δ.

We initially spun up a $dx = 1$ km simulation for 200 days, and then branched all other runs off this run, running for at least 50 days to allow adjustment to different resolutions. All quantities analyzed in this paper are averaged horizontally and over the last 5 days of simulation.

3 Hypothesis and Theory

3.1 Hypothesis for cloud fraction sensitivity

We now sketch a hypothetical explanation for the dramatic increase of cloud fraction with resolution seen in Fig. 1. Later sections of the paper will buttress this initial explanation with further evidence.

Equation (1) implies more effective mixing at higher resolutions, hence greater evaporation. Greater evaporation suggests a decrease in the *conversion efficiency* $(c - e)/c$ [*Langhans et al.*, 2015; *Lutsko and Cronin*, 2018], which is the fraction of condensate which turns to rain and is a vertically-resolved measure of precipitation efficiency. Since the non-interactive radiative cooling (2) fixes the amount of latent heating which convection must provide, a decrease in conversion efficiency implies that the convective mass flux must increase. But if mass fluxes go up, gross detrainment should too, leading to increased cloudiness. We summarize this hypothesis as

$$\begin{array}{ccccccccc} \text{Increased} \\ \text{evaporation} \end{array} \longrightarrow \begin{array}{c} \text{Decreased} \\ \text{PE} \end{array} \longrightarrow \begin{array}{c} \text{Increased} \\ \text{mass flux} \end{array} \longrightarrow \begin{array}{c} \text{Increased} \\ \text{detrainment} \end{array} \longrightarrow \begin{array}{c} \text{Increased} \\ \text{cloudiness} \end{array} . \tag{5}$$

Figure 2 shows that qualitatively, the above quantities (diagnosed as outlined in the previous section) behave as hypothesized. [add comment that connection between these quantities may be non-local in height?] But confidence in the hypothesis (5) requires *quantitative* confirmation of the proposed relationships, including the the basic scaling (1). These tasks will be taken up in the next sections, and will be facilitated by the theory of *Seeley et al.* [2019], which we describe next.

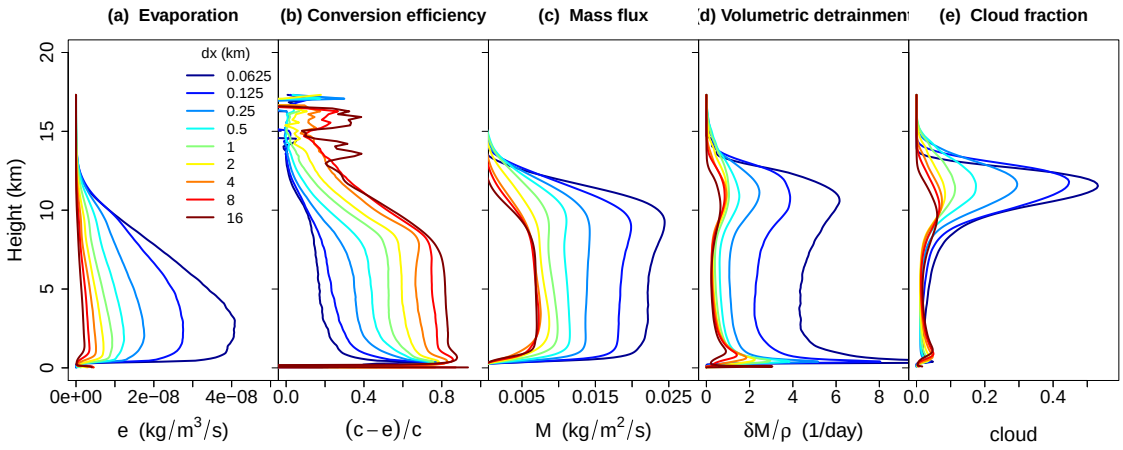

Figure 2. Increasing evaporation with resolution leads to increased cloud fraction These panels show the quantities appearing in the the hypothesis (5), as a function of both height and resolution dx. A qualitative consistency between the simulations and the hypothesis (5) is evident. All quantities are diagnosed as described in the main text.

3.2 Theory I: Cloud fraction as source times lifetime

To test the narrative in Eq. (5) we will employ the cloud-fraction theory of *Seeley et al.* [2019], hereafter S19. The theory consists of two major components. The first is a decomposition of cloud fraction C into a source times a lifetime, where the source is volumetric detrainment $\delta M/\rho$ and the lifetime $\tau_{\rm cld}$ represents the time it takes for a detrained, cloudy parcel to cease being cloudy (i.e. $q_{\rm c}<q_{\rm c0}$). Following S19 we write this as

$$C = \frac{\delta M}{\rho}\tau_{\rm cld} \ . \tag{6}$$

Since C and $\delta M/\rho$ are readily diagnosed as described above, one can then diagnose $\tau_{\rm cld}$ using (6); these quantities are plotted in Fig. 3. A few features are worth noticing. The first is that in the mid-troposphere, $\tau_{\rm cld}$ decreases markedly with resolution, which as discussed below is due to more efficient mixing and evaporation. In the upper troposphere, however, $\tau_{\rm cld}$ only varies by a factor of two or so, and does so non-monotonically with dx. Thus, changes in $\tau_{\rm cld}$ are not driving the dx-dependence of upper-tropospheric cloud fraction. From Eq. (6) we can then conclude that the increase of anvil cloud fraction with resolution must instead be due to increases in volumetric detrainment $\delta M/\rho$, as hypothesized in (5).

3.3 Theory II: Analytical model for cloud lifetime

The second component of the theory is an analytical model for the cloud lifetime $\tau_{\rm cld}$. Though we found above that changes in $\tau_{\rm cld}$ at the anvil height do not directly drive anvil cloud fraction changes, we will see below that the changes in $\tau_{\rm cld}$ in the mid-troposphere reflect the changes in mixing which do end up driving anvil cloud changes (as per the hypothesis (5)). In fact, combining the analytical model for $\tau_{\rm cld}$ with Eq. (6) will allow us to diagnose mixing timescales κ for each of our simulations, allowing us to test Eq. (1) which is a linchpin of our analysis.

The analytical model for $\tau_{\rm cld}$ begins with an ordinary differential equation for cloud condensate $q_{\rm c}$ in a detrained parcel, assuming that evaporation and warm-rain autoconversion

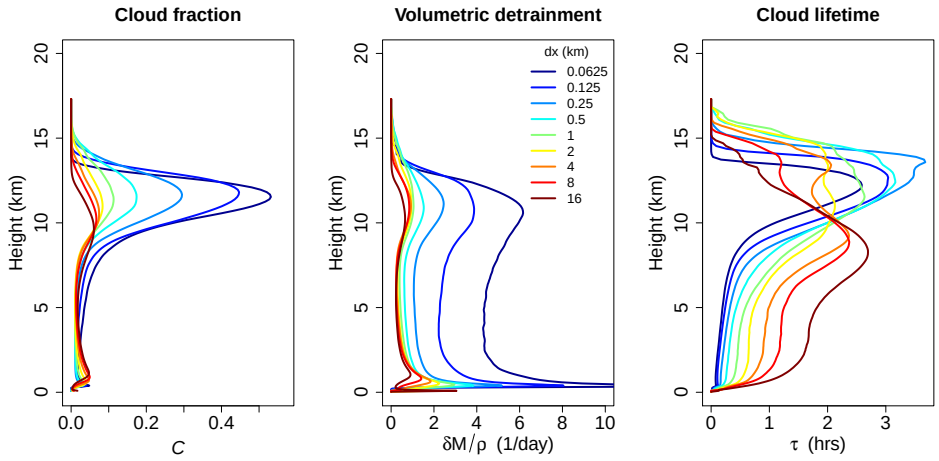

Figure 3. Cloud fraction changes are dominated by detrainment changes. These panels show the quantities appearing in Eq. (6), as a function of height and resolution. Since $\tau_{\rm cld}$ at the anvil level does not exhibit a strong trend with resolution, the strong trend in anvil cloud fraction with resolution is due to the trend in volumetric detrainment $\delta M/\rho$.

on a fixed timescale $t_{\rm aut}$ are the only sinks of cloud water:

$$\frac{dq_{\rm c}}{dt} = \underbrace{-\frac{1}{\kappa}\frac{1}{1+t/\kappa}[q_{\rm c}+(1-{\rm RH})q_{\rm v}^*]}_{\text{mixing}} - \underbrace{\frac{q_{\rm c}}{t_{\rm aut}}}_{\text{autoconversion}} . \tag{7}$$

The expression $q_{\rm c}+(1-{\rm RH})q_{\rm v}^*$ is the total water mass require to homogenize a unit mass of clear air that is mixed into the inactive cloudy air, while $1+t/\kappa$ is the mass of the parcel at time t relative to its initial (unit) mass, and $1/\kappa$ is the mixing rate. For a complete derivation of (7), see S19.

Equation (7) can be solved analytically, and an analytical formula for the lifetime $\tau_{\rm cld}$ at which $q_{\rm c} < q_{\rm c0}$ can be derived [Eqs. (A.2)]. This formula contains κ as an undetermined parameter, to be determined by optimization. We optimize κ by minimizing the RMSE between the simulated cloud fraction and that given by Eq. (6), where $\delta M/\rho$ is diagnosed directly from the simulations but $\tau_{\rm cld}$ is given by Eq. (A.2). The results of this optimization for each of our warm-rain (Kessler) simulations is shown in Fig. 4. One can see that for $dx > 0.5$ km or so, the S19 theory captures the simulated cloud fraction profiles reasonably well. For $dx \lesssim 0.5$ km the fit degrades, likely due to our neglect of anvil cloud spreading (Appendix A.2). What is of interest here, however, are the values for κ diagnosed from each of these fits, which are noted in each panel in Fig. 4 and also shown in Fig. 5. Fig. 5 also shows a linear fit of the form $\kappa = dx/u_{\rm rms}$. This figure shows that the scaling (1) is indeed consistent with our simulations and the S19 theory (which was used to diagnose κ). Furthermore, the $u_{\rm rms}$ value derived from the linear fit is 0.1 m/s, roughly consistent with the variations in horizontal velocity seen by inspection in our simulations.

4 Evaporation, PE, and mass flux

The last section presented evidence that simulated mixing increases with resolution following (1). But, how do we know that this mixing is behind the changes in evaporation manifest in Fig. 2a? And how do we know that these evaporation changes indeed cause the PE changes in Fig. 2b, and that these PE changes indeed driving the mass flux changes seen in Fig. 2c? We turn to these questions now.

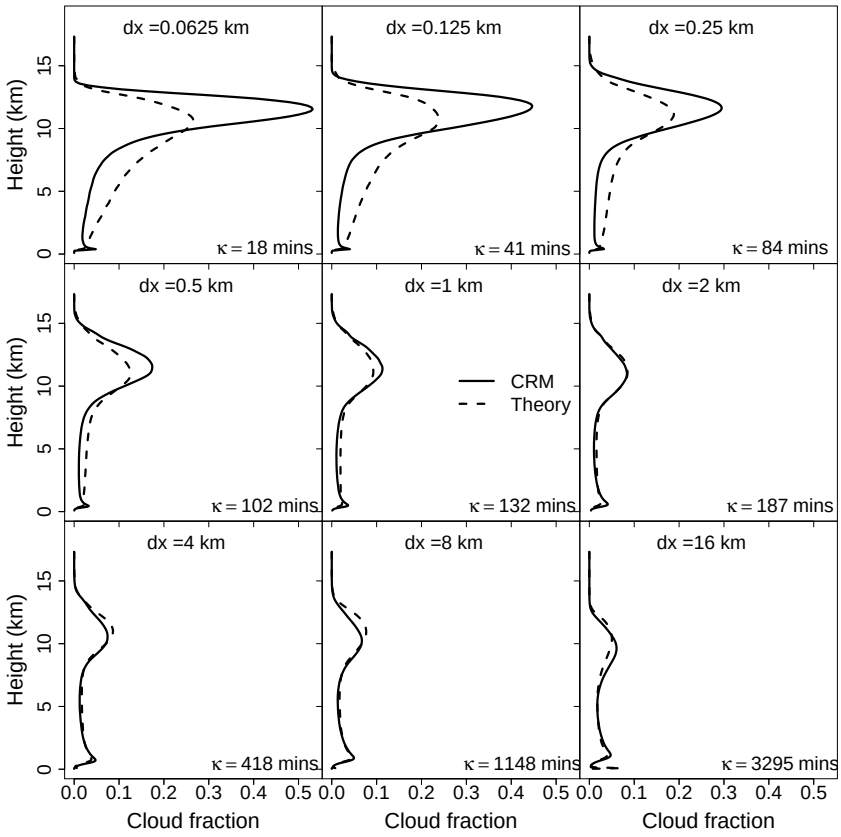

Figure 4. The S19 theory approximates the simulated cloud fraction, and diagnoses a dx-dependent κ. These panels show the simulated cloud fraction profile at a given resolution dx (solid lines), along with the prediction from the S19 theory [dashed lines, Eqs. (A.2) and (6)]. The S19 theory approximates the simulated cloud fraction profiles reasonably well for $dx \gtrsim 0.5$ km. The S19 theory also yields, via optimization, a value for κ at each dx, noted in the lower right of each panel.

To assess the influence of the mixing timescale κ on condensate evaporation, we note that by Eq. (7) the evaporation rate in the neighborhood of an updraft grid cell (neglecting inactive grid cells whose contribution in the mid and lower troposphere is small) should just be ρ times the mixing term. Averaging over the domain and invoking (1) (evaluated at $t = 0$ for simplicity) then yields

$$e = \frac{\rho u_{\rm rms}}{dx} \sigma_{\rm up} [q_{\rm c,up} + (1 - {\rm RH}) q_{\rm v}^*] \, . \tag{8}$$

We compare this estimate of evaporation to that diagnosed directly from our simulations in Fig. 6. Here $u_{\rm rms}$ was chosen to optimize the accuracy of the estimate (8), and gives $u_{\rm rms} = 0.2$ m/s, similar to the previous value. The agreement in Fig. 6a,b is reasonable, suggesting that Eq. (8) is indeed a good first-order description of the evaporation rate.

Equation (8) tells us that the evaporation rate e is proportional to dx, but also to the fractional updraft area $\sigma_{\rm up}$ which also increases with resolution (since $M \sim \sigma_{\rm up}$, cf. Fig. 2c). To confirm the central role of the dx-dependence in (8), Fig. 6c shows the evaporation rate e normalized by the mass flux M, which can be interpreted as the rate at which $q_{\rm c,up}$ decreases (due to evaporation) in a convecting parcel per unit height traveled. This quantity increases markedly with resolution, confirming that the proportionality between e and dx in (8) is a primary influence on evaporation rates.

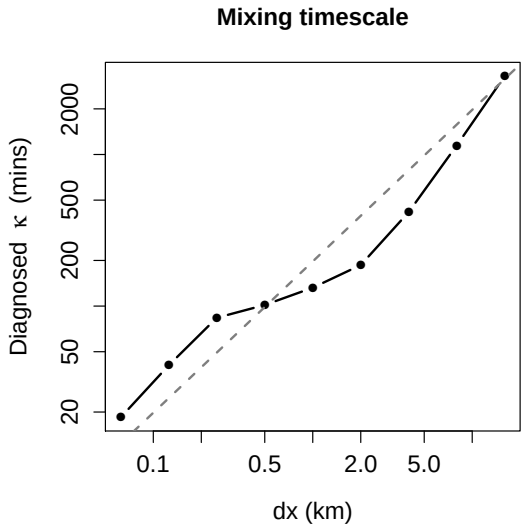

Figure 5. Diagnosed mixing timescale κ depends linearly on resolution This figure shows the values of κ diagnosed as in Fig. 4, as a function of dx (black dots and lines). Also shown is a linear fit of the form (1) with $u_{\rm rms} = 0.1$ m/s (gray line). The reasonable agreement supports the linear scaling (1).

How do these marked increases in evaporation, even measured relative to mass flux M, relate to the actual increases in M? The hypothesis (5) posits that this increase in mass flux is due to a decrease in precipitation efficiency PE from enhanced mixing. To check this connection, we calculate PE as precipitation P divided by vertically-integrated condensation, PE $\equiv P/\int c dz$, and also calculate a vertically-averaged $\langle M \rangle$ over 2 and 10 km (the range over which M in each simulation is roughly constant). From atmospheric energy balance, we expect that the fixed column integrated radiative cooling $Q = 120$ W/m^2 should equal PE times an estimated cloud base moisture flux of $Lq_{\rm v,bl}\langle M \rangle$, where the boundary-layer humidity $q_{\rm v,bl} = 0.017$ kg/kg is calculated as the time-mean lowest-level humidity averaged across all the simulations. This implies that $\langle M \rangle$ and PE should be related as

$$\langle M \rangle = \frac{Q}{Lq_{\rm v,bl}} \frac{1}{\rm PE} \, . \tag{9}$$

This relationship, along with $\langle M \rangle$ and PE calculated from the simulations, are shown in Figure 7. This figure shows that PE indeed decreases markedly as resolution increases, and that the corresponding increase in mass flux is indeed governed by the atmospheric energy balance as encapsulated in Eq. (9). This provides quantitative confirmation of parts of the mechanism proposed in Eq. (5), namely that more efficient evaporation reduces PE and hence increases M as resolution increases.

It should be noted here that PE includes both the vertical integral of the conversion efficiency shown in Fig. 2, as well as the *sedimentation efficiency* which measures the ratio of domain-integrated rain water production to surface rain rate [*Langhans et al.*, 2015; *Lutsko and Cronin*, 2018]. The sedimentation efficiency can differ from unity due to re-evaporation of rain, which is undiagnosed in our simulations. Future work will consider the sedimentation efficiency of these simulations, and the extent to which these PE changes are due to changes in conversion vs. sedimentation efficiency.

As an aside, we also note that the increase in evaporation and decrease in PE with resolution might also be expected to cause increases in relative humidity (RH). Indeed, such a relationship was explicitly formulated in *Romps* [2014]. While such changes in RH are not

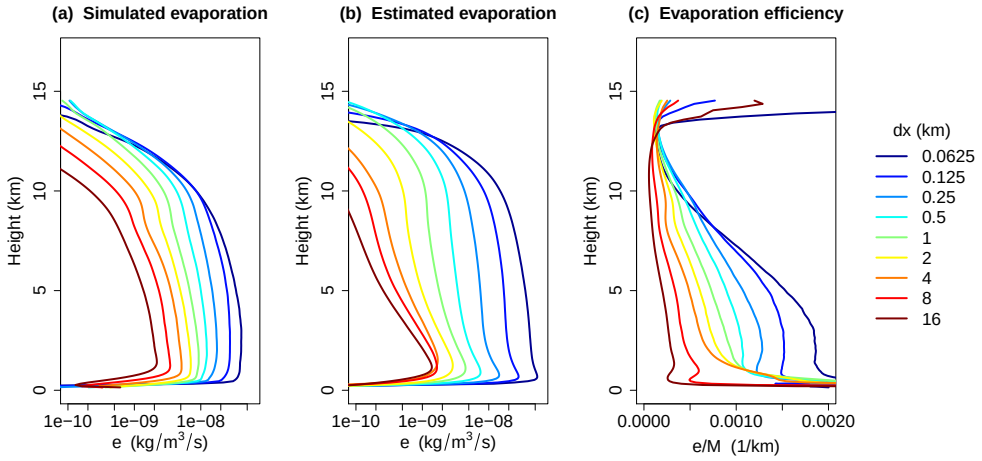

Figure 6. Evaporation scales as $1/dx$, as captured by Eq. (8). The vertically-resolved evaporation e diagnosed directly from our simulations (panel a) is well approximated by Eq. (8) (panel b). Normalizing evaporation by the mass flux profiles M (panel c) confirms that the $1/dx$ factor in Eq. (8) is influencing evaporation rates. Note the logarithmic x-axis in panels a,b.

directly relevant to the changes in cloud fraction which are the focus of this paper, they are straightforward to understand using the theory of *Romps* [2014] in conjunction with the diagnostics developed here. For completeness, this analysis is presented in Appendix B: .

5 Summary and Discussion

We summarize our main results as follows:

- Cloud-resolving simulations exhibit a marked increase of anvil cloud fraction with resolution (Fig. 1).
- This sensitivity can be traced to the resolution-dependence of evaporation and hence precipitation efficiency [Eq. (5), Figs. 2, 6, 7]
- The root of this sensitivity is that the mixing which causes evaporation scales linearly with resolution [Eq. (1), Fig. 5]

A key ingredient in this analysis was the theory of S19, which allowed us to diagnose values of the mixing timescale κ for each simulation and hence verify Eq. (1).

This work raises a number of questions and possible future research directions. Perhaps most saliently, what are the implications of these results for more realistic simulations? For regional or global simulations at $O(1-10\,\text{km})$ resolution with explicit convection [e.g. *Prein*, 2015; *Stevens et al.*, 2019], does the scaling (1) still hold, with similar consequences for precipitation efficiency? If so, what are the implications for rainfall rates at various spatiotemporal scales? Note that for transient forecast simulations the atmospheric energy constraint may not be relevant, and so the knock-on effects of PE on mass flux and cloud fraction may not occur, but the scalings (1) and (8) should hold at all timescales and still affect PE.

On climate timescales, *Zhao* [2014]; *Zhao et al.* [2016] found a close connection between gross precipitation efficiency and climate sensitivity for coarse-resolution models with parameterized convection. Does the same hold true for global climate models with explicit convection, such as global CRMs [*Satoh et al.*, 2019; *Stevens et al.*, 2019] or super-parameterized GCMs [*Khairoutdinov et al.*, 2005]? And if so, do the relationships between

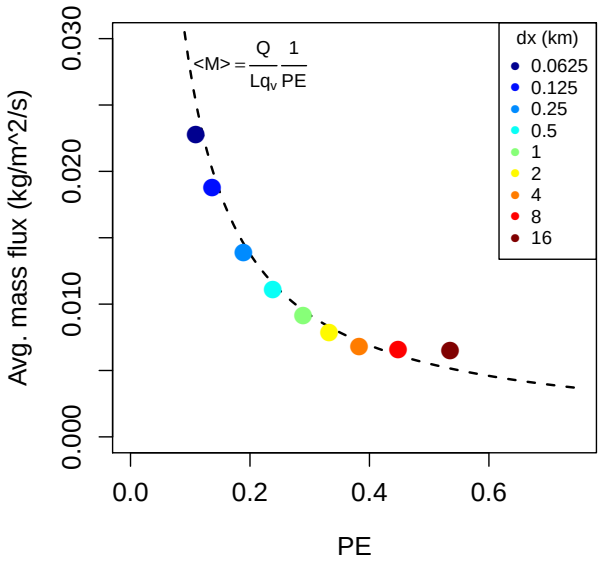

Figure 7. Mass fluxes increase with decreasing PE**, as dictated by energy balance.** This figure shows vertically-averaged mass-flux $\langle M \rangle$ plotted against precipitation efficiency PE, defined as precipitation divided by vertically-integrated condensation, for our simulations at varying dx (colored points). Also shown is the relationship (9), which is an expression of atmospheric energy balance (dashed line). A strong decrease of PE with dx is evident, and the mass flux covaries according to (9).

resolution, PE, and cloud fraction found here also operate in such models? If so, then one might expect a significant resolution dependence of PE, cloud fraction, and perhaps even climate sensitivity in such models, stemming from the simple scaling (1). As mentioned in the introduction, such a resolution sensitivity of convection-resolving global models would also complicate their use as benchmarks for machine learning.

Finally, it is worth commenting on why the resolution-dependence of cloudiness is somewhat unique relative to other resolution sensitivities. In some sense, a resolution sensitivity of cloudiness is not surprising because most aspects of atmospheric simulation, including wind fields, thermodynamic variables, and moisture variables, are sensitive to resolution to some degree. What is unique about cloud condensate, however – especially relative to other tracers – is that its sources and sinks are largely given by saturation adjustment, which is a threshold process and thus inherently nonlinear. This means that a change in mixing efficiency doesn't merely redistribute a conserved amount of condensate in space, as might be the case for other tracers; because of saturation adjustment, mixing can actually dramatically change how much condensate there *is*. Given the importance of clouds and precipitation to both weather and climate simulations, further study of how resolution, numerics, and subgrid mixing schemes affect cloud condensate in particular seems warranted.

A: Further details of the cloud lifetime model

A.1 Derivation of cloud lifetime

Equation (7) is a linear ordinary differential equation and can be solved by the usual method of finding particular and homogenous solutions and taking their sum. Upon impos-

ing the initial condition that the initial q_c value for the detrained parcel is simply the updraft value, i.e. $q_c(t=0) = q_{c,up}$, one obtains (see also S19)

$$q_c(t) = \frac{1}{1+t/\kappa}\left[q_{c,up}e^{-t/t_{aut}} - \frac{t_{aut}}{\kappa}(1-\mathrm{RH})q_v^*(1-e^{-t/t_{aut}})\right] . \tag{A.1}$$

The factor of $(1+t/\kappa)$ is just the volume at time t relative to the parcel's initial volume, and thus its appearance in the solution above represents the effect of dilution of condensate as the parcel's volume grows. The first term in brackets represents the decay of q_c due to the autoconversion sink, and the second term represents the effect of condensate evaporation into entrained, subsaturated environmental air.

With the solution (A.1) in hand it is straightforward, if slightly tedious, to solve for the time τ_{cld} at which $q_c = q_{c0}$. Employing the Lambert W function (which satisfies by definition $x = W(x)e^{W(x)}$) we have

$$\tau_{cld} = t_{aut}\left[W(ae^b) - b\right] \tag{A.2a}$$

where

$$a = \frac{\kappa}{t_{aut}}\frac{q_{c,up}}{q_{c0}} + \frac{(1-\mathrm{RH})q_v^*}{q_{c0}} \tag{A.2b}$$

$$b = \frac{\kappa}{t_{aut}} + \frac{(1-\mathrm{RH})q_v^*}{q_{c0}} \tag{A.2c}$$

A.2 Accounting for anvil spread

Multiplying τ_{cld} derived above by the volumetric detrainment as in (6) gives a time-mean cloud fraction, but assumes the cloud area stays fixed during its lifetime. Inspection of coarse-resolution ($dx \gtrsim 0.5$ km or so) simulations shows that this is a reasonable assumption, but at higher resolutions the anvils begin to spread before disappearing, potentially explaining the theory-CRM mismatch at high resolutions in Fig. 4. S19 incorporated anvil spreading into their model by integrating the cloud area $A(t) = A_0(1+t/\kappa)$ over time to obtain an *effective* cloud lifetime $\widetilde{\tau}_{cld}$:

$$\int_0^{\tau_{cld}} A_0(1+t/\kappa) = A_0\left(\tau_{cld} + \frac{\tau_{cld}^2}{2\kappa}\right) \equiv A_0\widetilde{\tau}_{cld} \tag{A.3a}$$

$$\text{where} \quad \widetilde{\tau}_{cld} = \tau_{cld} + \frac{\tau_{cld}^2}{2\kappa} . \tag{A.3b}$$

One then obtains an alternative theory for cloud fraction by substituting $\widetilde{\tau}_{cld}$ for τ_{cld} in Eq. (6). The predictions from this modified theory are shown in Fig. A.1. At coarser resolutions the modified cloud fraction profiles and associated κ values are quite similar to those in Fig. A.1. This is expected since at coarse resolutions $\kappa > \tau_{cld} \sim 150$ minutes (at the anvil level), so the additional term $\tau_{cld}^2/(2\kappa)$ in $\widetilde{\tau}_{cld}$ is not large compared to τ_{cld}. At finer resolutions (e.g. $dx = 0.125 - 0.25$ km), however, we have $\kappa < \tau_{cld}$ and now the modified theory predicts larger anvil cloud fractions for comparable κ, in better agreement with the CRM. The agreement in the mid-troposphere is worse, however, likely because mid-tropospheric clouds at fine resolution do not spread even though the upper-tropospheric anvils do. Finally, at 62.5 m the modified cloud fraction profile in Fig. A.1 agrees quite well with the CRM, in contrast to the mismatch in Fig. 4, but the diagnosed value $\kappa = 1$ minute is inconsistent with the value of 18 minutes found earlier in Figs. 4 and 5. The reasons for this are unclear.

B: Implications for Relative Humidity

The decreases in precipitation efficiency with resolution seen in the main text have implications for the environmental RH in our simulations, which we explore in this Appendix.

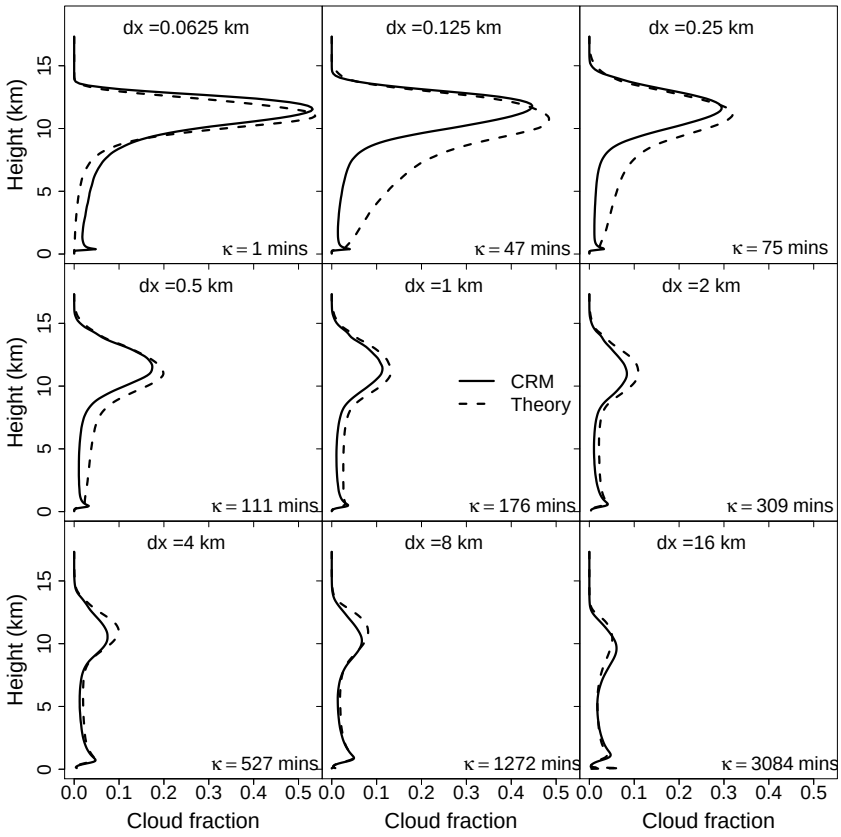

Figure A.1. Accounting for anvil spread improves predictions of anvil cloud fraction at high resolution, but degrades predictions of mid-tropospheric cloud fraction. As in Fig. 4, but using $\widetilde{\tau}_{\rm cld}$ from Eq. (A.3b) instead of $\tau_{\rm cld}$ in Eq. (6). Diagnosed κ values are similar to those in Fig. 4, except for the $dx = 0.0625$ km case.

Physically, one would expect that the increase in condensate evaporation per unit mass flux (Fig. 6c) would not only reduce PE, but would also lead to a moister environment and hence increased RH. These expectations may be quantified using the theory of *Romps* [2014] (hereafter R14), which provided expressions for RH both with and without evaporation, as encapsulated in the parameter $\alpha \equiv e/c$:

$$\text{RH} = \frac{\delta}{\gamma + \delta} \qquad \text{(no evap)} \tag{B.1a}$$

$$\text{RH} = \frac{\delta + \alpha\gamma - \alpha\epsilon}{\gamma + \delta - \alpha\epsilon} \quad \text{(with evap)} \, . \tag{B.1b}$$

Here δ is the gross fractional detrainment diagnosed from Eq. (4), $\gamma \equiv -d \ln q_{\rm v}^*/dz$ is the 'water-vapor lapse rate', and ϵ is the gross fractional entrainment rate diagnosed from the equation $\frac{1}{M}\frac{dM}{dz} = \epsilon - \delta$. Note that $\alpha = e/c$ is also just 1 minus the conversion efficiency shown in Fig. 2c, and also that (B.1b) reduces to (B.1a) if $\alpha = 0$. Equation (B.1a) expresses RH in terms of the competing processes of convective moistening (δ) and subsidence drying (γ), while (B.1b) includes the additional effects of detrained condensate evaporation (R14).

Figure B.1 shows profiles of RH calculated from Eq. (B.1a), Eq. (B.1b), and as diagnosed directly from the simulations. The simulated profiles show that RH increases markedly with horizontal resolution, with mid-tropospheric values ranging from 0.45 at $dx = 16$ km

to 0.9 at $dx = 62$ m. This RH increase is captured by Eq. (B.1b), but is much less consistent with the RH profiles predicted by Eq. (B.1a). This suggests that the PE decreases seen in Fig. 7 are largely driving the RH changes seen in Fig. B.1c, and that the latter are yet another impact of increased evaporation resulting from more efficient mixing at higher resolution. A caveat of these results is that rain re-evaporation should be included in the calculation of α but is currently omitted; Future work will assess the effect of this omission.

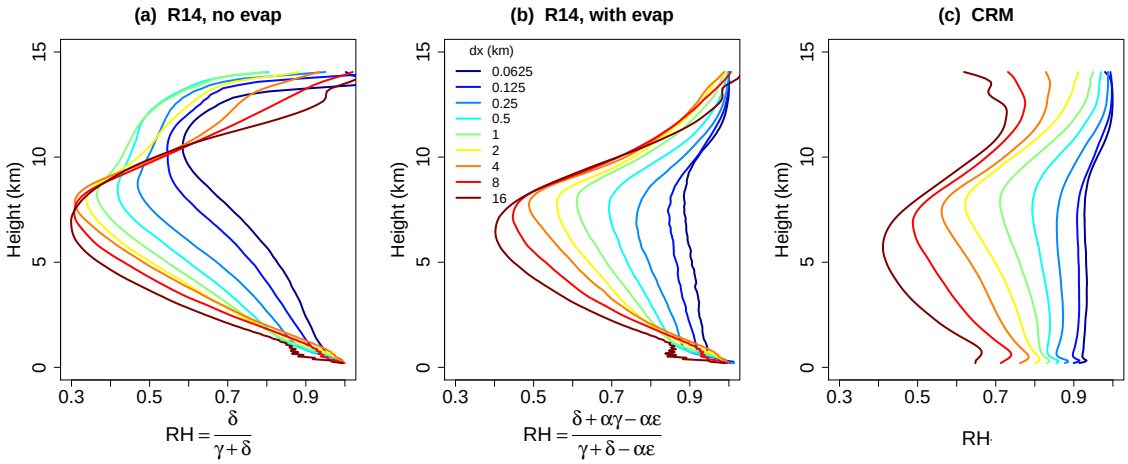

Figure B.1. Relative humidity increases markedly with resolution, driven largely by changes in PE These panels show RH profiles at varying resolutions as obtained **(a)** from Eq. (B.1a), **(b)** from Eq. (B.1b), **(c)** directly from the simulations. The simulated RH increases dramatically with resolution (panel c), and this increase is largely reproduced using Eq. (B.1b) which includes the effects of precipitation efficiency via the parameter $\alpha = e/c$ (panel b). Omitting PE effects by setting $\alpha = 0$ yields a noticeably worse approximation to the simulated RH profiles (panel a), suggesting that PE changes are a key driver in the resolution sensitivity of RH seen here.

Acknowledgments

NJ thanks Yi Ming, Ming Zhao, and V. Balaji for discussions.

References

Brenowitz, N. D., and C. S. Bretherton (2018), Prognostic Validation of a Neural Network Unified Physics Parameterization, *Geophysical Research Letters*, *45*(12), 6289–6298, doi:10.1029/2018GL078510.

Cesana, G., and H. Chepfer (2012), How well do climate models simulate cloud vertical structure? A comparison between CALIPSO-GOCCP satellite observations and CMIP5 models, *Geophysical Research Letters*, *39*(20), 1–6, doi:10.1029/2012GL053153.

Chen, J. H., and S. J. Lin (2013), Seasonal predictions of tropical cyclones using a 25-km-resolution general circulation model, *Journal of Climate*, *26*(2), 380–398, doi:10.1175/JCLI-D-12-00061.1.

Cronin, T. W., and A. A. Wing (2017), Clouds, Circulation, and Climate Sensitivity in a Radiative-Convective Equilibrium Channel Model, *Journal of Advances in Modeling Earth Systems*, pp. 2883–2905, doi:10.1002/2017MS001111.

Dinh, T. P., D. R. Durran, and T. P. Ackerman (2010), Maintenance of tropical tropopause layer cirrus, *Journal of Geophysical Research Atmospheres*, *115*(D2), 1–15, doi:10.1029/2009JD012735.

Durran, D. R., T. Dinh, M. Ammerman, and T. Ackerman (2009), The mesoscale dynamics of thin tropical tropopause cirrus, *Journal of the Atmospheric Sciences*, *66*(9), 2859–2873, doi:10.1175/2009JAS3046.1.

Garrett, T. J., B. C. Navarro, C. H. Twohy, E. J. Jensen, D. G. Baumgardner, P. T. Bui, H. Gerber, R. L. Herman, A. J. Heymsfield, P. Lawson, P. Minnis, L. Nguyen, M. Poellot, S. K. Pope, F. P. J. Valero, and E. M. Weinstock (2005), Evolution of a Florida Cirrus Anvil, *Journal of the Atmospheric Sciences*, *62*(7), 2352–2372, doi:10.1175/JAS3495.1.

Garrett, T. J., M. A. Zulauf, and S. K. Krueger (2006), Effects of cirrus near the tropopause on anvil cirrus dynamics, *Geophysical Research Letters*, *33*(17), 1–5, doi:10.1029/2006GL027071.

Harris, L. M., and S.-J. Lin (2013), A Two-Way Nested Global-Regional Dynamical Core on the Cubed-Sphere Grid, *Monthly Weather Review*, *141*(1), 283–306, doi:10.1175/MWR-D-11-00201.1.

Harrop, B. E., and D. L. Hartmann (2012), Testing the role of radiation in determining tropical cloud-top temperature, *Journal of Climate*, *25*(17), 5731–5747, doi:10.1175/JCLI-D-11-00445.1.

Hartmann, D. L., and K. Larson (2002), An important constraint on tropical cloud - climate feedback, *Geophysical Research Letters*, *29*(20), 1951, doi:10.1029/2002GL015835.

Hartmann, D. L., L. A. Moy, and Q. Fu (2001), Tropical convection and the energy balance at the top of the atmosphere, *Journal of Climate*, *14*(24), 4495–4511, doi:10.1175/1520-0442(2001)014<4495:TCATEB>2.0.CO;2.

Hartmann, D. L., B. Gasparini, S. E. Berry, and P. N. Blossey (2018), The Life Cycle and Net Radiative Effect of Tropical Anvil Clouds, *Journal of Advances in Modeling Earth Systems*, *10*(12), 3012–3029, doi:10.1029/2018MS001484.

Jeevanjee, N. (2017), Vertical velocity in the gray zone, *Journal of Advances in Modeling Earth Systems*, *9*, 2304–2316, doi:10.1002/2017MS001059.

Jeevanjee, N., and D. M. Romps (2018), Mean precipitation change from a deepening troposphere, *Proceedings of the National Academy of Sciences*, *115*(45), 11,465–11,470, doi:10.1073/pnas.1720683115.

Jeevanjee, N., P. Hassanzadeh, S. Hill, and A. Sheshadri (2017), A perspective on climate model hierarchies, *Journal of Advances in Modeling Earth Systems*, *9*(4), 1760–1771, doi:10.1002/2017MS001038.

Kessler, E. (1969), *On the distribution and continuity of water substance on atmospheric circulation*, vol. 10, 84 pp., American Meteorological Society, Boston, MA, doi:http://dx.doi.org/10.1016/0169-8095(94)00090-Z.

Khairoutdinov, M., D. Randall, and C. DeMott (2005), Simulations of the atmospheric general circulation using a cloud-resolving model as a superparameterization of physical processes, *Journal of the Atmospheric Sciences*, *62*(7 I), 2136–2154, doi:10.1175/JAS3453.1.

Langhans, W., K. Yeo, and D. M. Romps (2015), Lagrangian Investigation of the Precipitation Efficiency of Convective Clouds, *Journal of the Atmospheric Sciences*, *72*(3), 1045–1062, doi:10.1175/JAS-D-14-0159.1.

Lin, S.-J. (2004), A 'Vertically Lagrangian' Finite-Volume Dynamical Core for Global Models, *Monthly Weather Review*, *132*(10), 2293–2307, doi:10.1175/1520-0493(2004)132<2293:AVLFDC>2.0.CO;2.

Lindzen, R. S., M. D. Chou, and A. Y. Hou (2001), Does the Earth Have an Adaptive Infrared Iris?, *Bulletin of the American Meteorological Society*, *82*(3), 417–432, doi:10.1175/1520-0477(2001)082<0417:DTEHAA>2.3.CO;2.

Lutsko, N. J., and T. W. Cronin (2018), Increase in Precipitation Efficiency With Surface Warming in Radiative-Convective Equilibrium, *Journal of Advances in Modeling Earth Systems*, *10*(11), 2992–3010, doi:10.1029/2018MS001482.

Mauritsen, T., and B. Stevens (2015), Missing iris effect as a possible cause of muted hydrological change and high climate sensitivity in models, *Nature Geoscience*, *8*(April), 8–13, doi:10.1038/ngeo2414.

Narenpitak, P., C. S. Bretherton, and M. F. Khairoutdinov (2017), Cloud and circulation feedbacks in a near-global aquaplanet cloud-resolving model, *Journal of Advances in Modeling Earth Systems*, *9*, 1069–1090, doi:10.1002/2016MS000872.Received.

Prein, A. F. (2015), A review on regional convection-permitting climate modeling: Demonstrations, prospects, and challenges, *Reviews of Geophysics*, pp. 1–39, doi:10.1002/2014RG000475.Received.

Rasp, S., M. S. Pritchard, and P. Gentine (2018), Deep learning to represent subgrid processes in climate models., *Proceedings of the National Academy of Sciences of the United States of America*, *115*(39), 9684–9689, doi:10.1073/pnas.1810286115.

Romps, D. M. (2008), The Dry-Entropy Budget of a Moist Atmosphere, *Journal of the Atmospheric Sciences*, *65*(12), 3779–3799, doi:10.1175/2008JAS2679.1.

Romps, D. M. (2014), An Analytical Model for Tropical Relative Humidity, *Journal of Climate*, *27*(19), 7432–7449, doi:10.1175/JCLI-D-14-00255.1.

Romps, D. M. (2020), Climate Sensitivity and the Direct Effect of Carbon Dioxide in a Limited-Area Cloud-Resolving Model, *Journal of Climate*, *33*(9), 3413–3429, doi:10.1175/jcli-d-19-0682.1.

Satoh, M., B. Stevens, F. Judt, M. Khairoutdinov, S.-j. Lin, W. M. Putman, and P. Düben (2019), Global Cloud-Resolving Models, *Current Climate Change Reports*, *5*, 172–184.

Schmidt, C. T., and T. J. Garrett (2013), A Simple Framework for the Dynamic Response of Cirrus Clouds to Local Diabatic Radiative Heating, *Journal of the Atmospheric Sciences*, *70*(5), 1409–1422, doi:10.1175/JAS-D-12-056.1.

Seeley, J. T., N. Jeevanjee, W. Langhans, and D. M. Romps (2019), Formation of Tropical Anvil Clouds by Slow Evaporation, *Geophysical Research Letters*, *46*(1), 492–501, doi:10.1029/2018GL080747.

Sherwood, S. C., M. J. Webb, J. D. Annan, K. C. Armour, P. M. Forster, J. C. Hargreaves, G. Hegerl, S. A. Klein, K. D. Marvel, E. J. Rohling, M. Watanabe, T. Andrews, P. Braconnot, C. S. Bretherton, G. L. Foster, Z. Hausfather, A. S. Heydt, R. Knutti, T. Mauritsen, J. R. Norris, C. Proistosescu, M. Rugenstein, G. A. Schmidt, K. B. Tokarska, and M. D. Zelinka (2020), An Assessment of Earth's Climate Sensitivity Using Multiple Lines of Evidence, *Reviews of Geophysics*, *58*(4), 1–92, doi:10.1029/2019rg000678.

Singh, M. S., and P. A. O'Gorman (2015), Increases in moist-convective updraught velocities with warming in radiative-convective equilibrium, *Quarterly Journal of the Royal Meteorological Society*, *141*(692), 2828–2838, doi:10.1002/qj.2567.

Stevens, B., M. Satoh, L. Auger, J. Biercamp, C. S. Bretherton, X. Chen, P. Düben, F. Judt, M. Khairoutdinov, D. Klocke, C. Kodama, L. Kornblueh, S. J. Lin, P. Neumann, W. M. Putman, N. Röber, R. Shibuya, B. Vanniere, P. L. Vidale, N. Wedi, and L. Zhou (2019), DYAMOND: the DYnamics of the Atmospheric general circulation Modeled On Non-hydrostatic Domains, *Progress in Earth and Planetary Science*, *6*(1), doi:10.1186/s40645-019-0304-z.

Su, H., J. H. Jiang, C. Zhai, V. S. Perun, J. T. Shen, A. Del Genio, L. S. Nazarenko, L. J. Donner, L. Horowitz, C. Seman, C. Morcrette, J. Petch, M. Ringer, J. Cole, K. Von Salzen, M. D. Mesquita, T. Iversen, J. E. Kristjansson, A. Gettelman, L. Rotstayn, S. Jeffrey, J. L. Dufresne, M. Watanabe, H. Kawai, T. Koshiro, T. Wu, E. M. Volodin, T. L'Ecuyer, J. Teixeira, and G. L. Stephens (2013), Diagnosis of regime-dependent cloud simulation errors in CMIP5 models using "a-Train" satellite observations and reanalysis data, *Journal of Geophysical Research Atmospheres*, *118*(7), 2762–2780, doi:10.1029/2012JD018575.

Tsushima, Y., S. I. Iga, H. Tomita, M. Satoh, A. T. Noda, and M. J. Webb (2014), High cloud increase in a perturbed SST experiment with a global nonhydrostatic model including explicit convective processes, *Journal of Advances in Modeling Earth Systems*, *6*(3), 571–585, doi:10.1002/2013MS000301.

Williams, I. N., and R. T. Pierrehumbert (2017), Observational evidence against strongly stabilizing tropical cloud feedbacks, *Geophysical Research Letters*, *44*(3), 1503–1510, doi:10.1002/2016GL072202.

Wing, A. A., C. L. Stauffer, T. Becker, K. A. Reed, M. Ahn, N. P. Arnold, S. Bony, M. Branson, G. H. Bryan, J. Chaboureau, S. R. Roode, K. Gayatri, C. Hohenegger, I. Hu, F. Jansson, T. R. Jones, M. Khairoutdinov, D. Kim, Z. K. Martin, S. Matsugishi, B. Medeiros, H. Miura, Y. Moon, S. K. Müller, T. Ohno, M. Popp, T. Prabhakaran, D. Randall, R. RiosâĂŘBerrios, N. Rochetin, R. Roehrig, D. M. Romps, J. H. Ruppert, M. Satoh, L. G. Silvers, M. S. Singh, B. Stevens, L. Tomassini, C. C. Heerwaarden, S. Wang, and M. Zhao (2020), Clouds and Convective Self-Aggregation in a Multi-Model Ensemble of Radiative-Convective Equilibrium Simulations, *Journal of Advances in Modeling Earth Systems*, pp. 1–72, doi:10.1029/2020ms002138.

Yuval, J., and P. A. O'Gorman (2020), Stable machine-learning parameterization of subgrid processes for climate modeling at a range of resolutions, *Nature Communications*, *11*(1), doi:10.1038/s41467-020-17142-3.

Zelinka, M. D., C. Zhou, and S. A. Klein (2016), Insights from a refined decomposition of cloud feedbacks, *Geophysical Research Letters*, *43*(17), 9259–9269, doi:10.1002/2016GL069917.

Zhao, M. (2014), An investigation of the connections among convection, clouds, and climate sensitivity in a global climate model, *Journal of Climate*, *27*(5), 1845–1862, doi:10.1175/JCLI-D-13-00145.1.

Zhao, M., J. C. Golaz, I. M. Held, V. Ramaswamy, S. J. Lin, Y. Ming, P. Ginoux, B. Wyman, L. J. Donner, D. Paynter, and H. Guo (2016), Uncertainty in model climate sensitivity traced to representations of cumulus precipitation microphysics, *Journal of Climate*, *29*(2), 543–560, doi:10.1175/JCLI-D-15-0191.1.

Zhou, L., S. J. Lin, J. H. Chen, L. M. Harris, X. Chen, and S. L. Rees (2019), Toward convective-scale prediction within the next generation global prediction system, *Bulletin of the American Meteorological Society*, *100*(7), 1225–1243, doi:10.1175/BAMS-D-17-0246.1.